Simulated Changes in Storm Morphology Associated with a Sea-Breeze Air Mass

JOSHUA HARTIGAN,[a] ROBERT A. WARREN,[b,c] JOSHUA S. SODERHOLM,[d] AND HARALD RICHTER[d]

[a] *School of Mathematical and Physical Sciences, University of Technology Sydney, Ultimo, New South Wales, Australia*
[b] *School of Earth, Atmosphere and Environment, Monash University, Melbourne, Victoria, Australia*
[c] *ARC Centre of Excellence for Climate Extremes, Monash University, Melbourne, Victoria, Australia*
[d] *Research Program, Australian Bureau of Meteorology, Melbourne, Victoria, Australia*

(Manuscript received 28 February 2020, in final form 2 September 2020)

ABSTRACT: The central east coast of Australia is frequently impacted by large hail and damaging winds associated with severe convective storms, with individual events recording damages exceeding AUD 1 billion. These storms present a significant challenge for forecasting because of their development in seemingly marginal environments. They often have been observed to intensify upon approaching the coast, with case studies and climatological analyses indicating that interactions with the sea breeze are key to this process. The relative importance of the additional lifting and vorticity along the sea-breeze front in comparison with the change to a cooler, moister air mass with stronger low-level shear behind the front has yet to be investigated. Here, the role of the sea-breeze air mass is isolated using idealized numerical simulations of storms developing in a horizontally homogeneous environment. The base-state substitution (BSS) modeling technique is utilized to introduce the sea-breeze air mass following initial storm development. Relative to a simulation without BSS, the storm is longer lived and more intense, ultimately developing supercell characteristics including increased updraft rotation, deviant motion to the left of the mean wind vector, and a strong reflectivity gradient on the inflow edge. Separately simulating the changes in the thermodynamic and wind fields reveals that the enhanced storm longevity and intensity are primarily due to the latter. The change in the low-level environmental winds slows gust-front propagation, allowing the storm to continue to ingest warm, potentially buoyant environmental air. At the same time, increased low-level shear promotes the development of persistent updraft rotation that causes the storm to make a transition from a multicell to a supercell.

KEYWORDS: Hail; Sea breezes; Severe storms; Supercells; Cloud resolving models

1. Introduction

Severe convective storms pose a serious threat to life, property, and infrastructure in many parts of the world. In Australia, this threat is strongly felt along the central east coast where severe storms bring large hail, damaging wind gusts, and occasional tornadoes. When these storms impact major coastal cities, they can result in extremely costly natural disasters. Examples of such events in Australia include the 1999 Sydney hailstorm (Buckley et al. 2001) and the 2014 Brisbane hailstorm (Soderholm et al. 2017b), both causing over AUD 1 billion in damage, with the former event remaining the costliest natural disaster to affect Australia to date (McAneney et al. 2016).

Relative to the Great Plains of the United States, the east coast of Australia represents a less favorable environment for severe storms. While significant buoyancy (CAPE $> 1000\,\mathrm{J\,kg^{-1}}$) is regularly observed during the warm season, wind shear profiles at this time tend to be only marginally supportive of rotating updrafts (average 0–6-km bulk wind difference of approximately $15\,\mathrm{m\,s^{-1}}$ during the Australian storm season; Allen and Karoly 2014). Another key difference is the existence of significant surface heterogeneity, associated with the Great Dividing Range, the coastline itself, and pronounced variations in land use and vegetation cover. This sets the stage for the development of thermally driven mesoscale circulations and associated airmass boundaries that can initiate and interact with convective storms. In particular, the sea breeze (SB; e.g., Miller et al. 2003) and its associated airmass boundary, the sea-breeze front (SBF), are ubiquitous features during the warm season when most severe storms occur. Previous case studies (Sills et al. 2004; Richter et al. 2014; Soderholm et al. 2017b) and climatological analyses (Soderholm et al. 2017a) suggest that, in certain situations, storms may undergo rapid intensification as they move into the SB air mass. This can lead to severe weather in the densely populated coastal zone with little lead time for disseminating warnings. An improved understanding of the interaction between convective storms and the SB would therefore be of great value to forecasters in this region.

There are two ways that airmass boundaries can impact storms. One way is through interaction with the boundary and its associated circulation. Horizontal convergence along boundaries such as the SBF promotes low-level lifting, that acts as a triggering mechanism for deep convection (Wilson and Megenhardt 1997; Wissmeier et al. 2010) and may augment the low-level updraft of an existing storm. In addition, baroclinically generated horizontal vorticity associated with the boundary can augment environmental horizontal vorticity, enhancing updraft rotation (Atkins et al. 1999; Rasmussen et al. 2000). Supercells interacting with boundaries have been found to produce stronger, longer-lived mesocyclones than those in an environment containing no boundary (Atkins et al. 1999). This increased rotation within the updraft can enhance updraft strength due to dynamic lifting associated with the vertical perturbation pressure gradient force

Corresponding author: Joshua Hartigan, joshua.hartigan@student.uts.edu.au

DOI: 10.1175/MWR-D-20-0069.1

(Weisman and Klemp 1984). Further, both observational and modeling studies have found supercells to be longer lived when interacting with a boundary (Maddox et al. 1980; Atkins et al. 1999; Bunkers et al. 2006). Boundaries can even provide a means by which long-lived supercells can exist in environments that are characterized by suboptimal vertical shear (Bunkers et al. 2006).

The second way airmass boundaries can impact storms is through changes in the airmass characteristics across the boundary. Convective storms are highly sensitive to variations in the ambient thermodynamic and wind profiles (Richardson et al. 2007; Ziegler et al. 2010). A number of idealized numerical simulations have been conducted in the past to investigate the effects that a varying environment has on an existing storm (e.g., Richardson et al. 2007; Bunkers 2010; Coffer and Parker 2015; Davenport and Parker 2015). Richardson et al. (2007) for example, found storms can become increasingly organized as they move into a stronger shear environment after having initiated in an environment characterized by weak shear. A changing wind and/or thermodynamic profile has also been found to impact the source region of inflow parcels (Davenport and Parker 2015). Although supercells might continue to draw some inflow from the surface of a moderately stable boundary layer, their updrafts weaken in the absence of increasing shear (Nowotarski et al. 2011). Increasing static stability might lead to storm demise; however, this can be partially offset by a concurrent increase in low-level shear through enhanced rotation and dynamic lifting (Coffer and Parker 2015) or by cold-pool lifting (Billings and Parker 2012).

The location of a storm relative to a boundary is also important as it can affect the source of storm inflow parcels (Atkins et al. 1999; Bunkers et al. 2006). As compared with supercells propagating in a cooler air mass, storms can be enhanced by moving along a boundary through ingesting more vorticity rich air, while increased buoyancy can enhance storms that move into a warmer air mass (Atkins et al. 1999; Bunkers et al. 2006). Ziegler et al. (2010) showed that supercell storms may weaken as they move into increasingly cool boundary layer air, due to deceleration of the gust front and an associated reduction in low-level lifting. This contrasts to some degree with what has been observed along the central east coast of Australia, where high-impact storm events are occasionally observed to intensify after moving into an SB air mass (Richter et al. 2014; Soderholm et al. 2017b).

Focusing on the southeast Queensland region of Australia, Soderholm et al. (2017a) suggested that the SB may be a major contributor to both the initiation and development of hailstorms. In an observational study of the 2014 Brisbane hailstorm, Soderholm et al. (2017b) found that the SB preconditioned the coastal environment for storms through enhancing low-level moisture and shear. While CIN within the SB air mass was higher, CAPE was also increased due to the greater dewpoint temperature and might be further enhanced locally through mixing with the urban heat island of Brisbane. Soderholm et al. (2017b) hypothesized that the storm intensified as a result of ingesting more potentially buoyant air from within the SB air mass.

To gain a better picture of storm sensitivity in coastal environments, this study aims to isolate the effects of the SB air mass on a preexisting storm from the effects of the SBF. Idealized numerical simulations are performed, utilizing pre- and post-SB airmass conditions to gain a deeper understanding of how the air mass affects storm morphology and longevity. Section 2 provides an outline of the simulations performed, including how the post-SB air mass was introduced. Results from these experiments, including nine sensitivity tests, are presented in section 3. A summary and discussion of these results are provided in section 4.

2. Methods

a. Model configuration

Numerical simulations were performed using the cloud model CM1, version 18 (Bryan and Fritsch 2002; Bryan 2017). The model was configured to solve the compressible governing equations on a three-dimensional domain of size 300 km × 200 km × 20 km, with uniform horizontal grid spacing of $\Delta x = \Delta y = 500$ m. The vertical grid was stretched, with Δz increasing from 50 m at the surface to 500 m above 12 km, resulting in a total of 76 levels. Rayleigh damping was applied to the uppermost 4 km of the model to limit the spurious reflection of wave energy. The lateral boundaries were open-radiative following the formulation of Durran and Klemp (1983), and both upper and lower boundaries were free-slip. The restricted outward flux option was enabled to prevent domain-total mass loss and pressure falls.

A vertically implicit Klemp–Wilhelmson (Klemp and Wilhelmson 1978) time-splitting scheme was used for temporal integration with 6 acoustic time steps per full time step of 3 s. An implicitly diffusive, fifth-order advection scheme was applied both horizontally and vertically with no additional artificial diffusion applied. Subgrid turbulence was parameterized using a turbulent kinetic energy scheme after Deardorff (1980), as outlined in Bryan (2017). Microphysical processes were represented using the double-moment scheme of Morrison et al. (2005) with hail (rather than graupel) used for the rimed ice category. To test sensitivity to microphysics schemes, further simulations were conducted using both the Thompson and NASA–Goddard microphysics schemes. The different schemes resulted in stronger cold pools during the control simulation (not shown) that led to storm decay prior to the introduction of the SB air mass. As such, the results from these different microphysics simulations cannot be adequately compared to the main results of this paper. The Coriolis force, friction, radiation, and surface fluxes were all neglected and no terrain was included. Storms were initiated in a horizontally homogeneous environment using a warm bubble centered at an altitude of 1.4 km, with horizontal and vertical radii of 10 and 1.4 km, respectively, and a maximum potential temperature perturbation of 3 K. All simulations were run for a total of 3.5 h, with output files produced every 5 min.

b. Initial conditions

Three fundamental storm environments were simulated: one that contained no SB air mass (CTRL), a modified SB air mass (SB1K), and an unmodified SB air mass (SB2K). The thermodynamic soundings for the primary simulations are

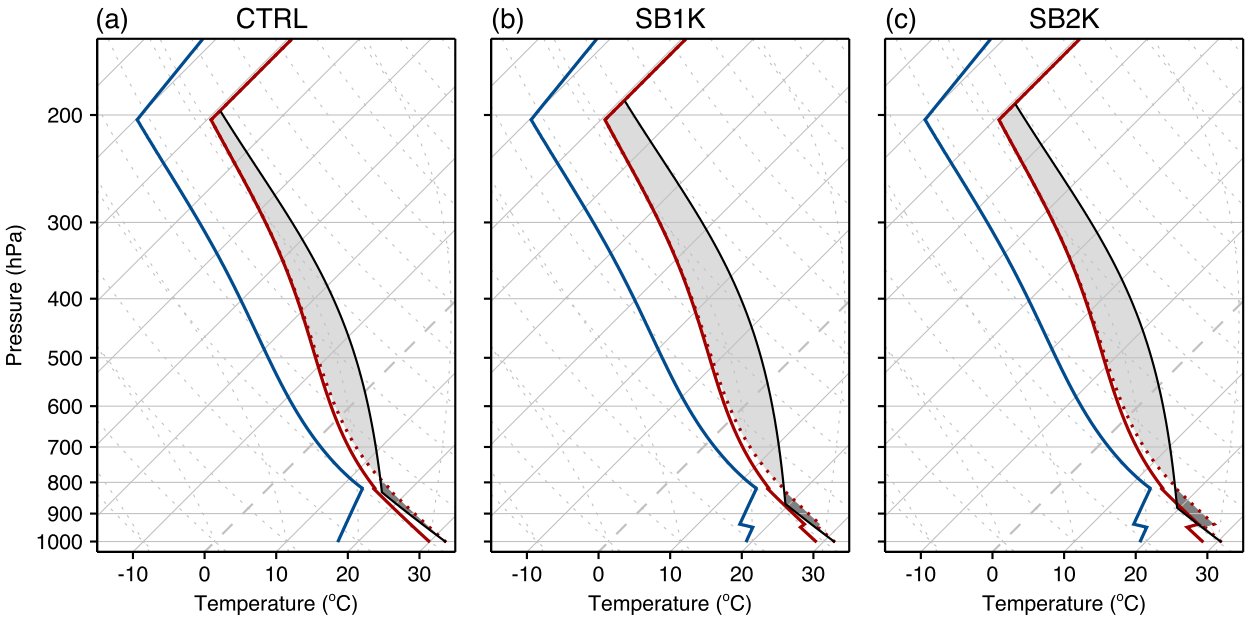

FIG. 1. Skew T–log$p$ diagrams for the (a) CTRL, (b) SB1K, and (c) SB2K simulations. Thick solid lines show the environmental temperature (red) and dewpoint temperature (blue), and the thick red dotted line represents environmental virtual temperature. The thin solid line shows the virtual temperature of a parcel lifted from the surface, with areas of positive and negative buoyancy shaded light and dark gray, respectively.

presented in Fig. 1, and hodographs representing the wind profiles of the primary simulations and additional sensitivity simulations (described below) are presented in Fig. 2. SB1K and SB2K will be referred to collectively as the SB simulations. The parameters to construct the initial boundary layer temperature and dewpoint temperature profiles for the CTRL simulation, following the method of Warren et al. (2017), were chosen to reproduce the 0200 UTC (1200 AEST) sounding from Kalbar in southeast Queensland on 27 November 2014 (Soderholm et al. 2017b, their Fig. 14). The vertical profiles of potential temperature and mixing ratio were derived on the basis of the 10 parameters specified in Table 1. The thermodynamic soundings for the SB air masses were created based on the CTRL sounding by decreasing and increasing the temperature and dewpoint temperature, respectively, by a fixed amount in the lowest 500 m. A 100-m transition layer was located above this, where the temperature and dewpoint temperature were calculated via linear interpolation between the original and modified profiles. The SB1K sounding corresponded to a warmed SB air mass with a temperature change of only −1 K, while the SB2K sounding contained a temperature change of −2 K, typical of an unmodified SB air mass on the coast (Soderholm et al. 2017b, their Fig. 9). Both soundings contained a dewpoint temperature change of +2 K. Thermodynamic and wind parameters relevant to the simulations are provided in Table 2. Thermodynamic parameters were calculated using a surface-based parcel and discussion herein refers to surface-based parcels. Because the potential temperature and mixing ratio are almost constant in the lowest 500 m of all simulations, the 500-m mixed-layer parcel values only vary slightly from the surface-based values. The resulting initial environment featured CAPE (calculated using the virtual temperature correction; Doswell and Rasmussen 1994) of 1500 J kg^{-1}, CIN of 49 J kg^{-1}, and an LCL of 1641 m. For SB1K, both CAPE and CIN increased to 2271 and 52 J kg^{-1}, respectively, while the LCL decreased to 1266 m relative to the CTRL. Meanwhile, for SB2K both CAPE and CIN increased to 2024 and 80 J kg^{-1}, respectively, while the LCL decreased to 1141 m.

The initial wind profile was created by specifying wind speed and direction (measured clockwise from due north) at the four or five levels outlined in Table 3, converting to their u and v components, and linearly interpolating between these values. There is an additional level at 500 m for SB1K and SB2K to specify the change in winds below 500 m associated with the SB air mass, whereas the winds in the CTRL vary linearly between the surface and 1 km. The low-level (0–3 km) profile is based on the composite morning (2300 UTC) sounding for SB days from Soderholm et al. (2017b, their Fig. 8) and features anticlockwise turning with weak speed shear. Unidirectional flow is assumed above 3 km, with wind speeds increasing to 30 m s^{-1} at the tropopause and remaining constant thereafter (Fig. 2). The 0–6-km bulk wind difference (BWD) specified by this environment is 15.5 m s^{-1}, and 0–3-km storm relative helicity (calculated using storm motion; see section 3) is −45 m^2 s^{-2} (Table 2). For the SB simulations, the easterly component of the low-level wind profile was enhanced to be representative of the change in wind speed and direction associated with an SB air mass (Table 3 and Fig. 2). This increased the magnitude of the 0–6-km BWD and 0–3-km storm relative helicity to 19.3 m s^{-1} and −64 m^2 s^{-2}, for SB1K and 19.3 m s^{-1} and −61 m^2 s^{-2} for SB2K, respectively (Table 2).

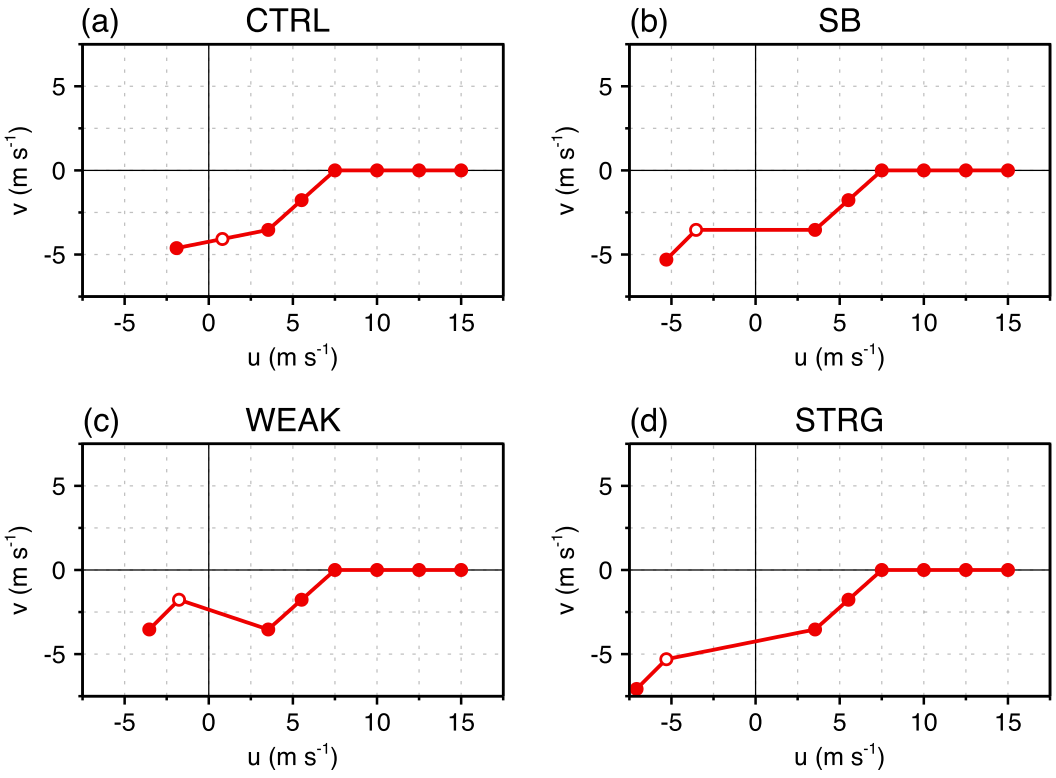

FIG. 2. Hodographs displaying the wind configuration in the lowest 6 km for the (a) CTRL, (b) SB, (c) WEAK, and (d) STRG simulations. TH1K and TH2K follow the hodograph in (a), and WIND, EARL, LATE, INST, and LONG follow the profile in (b). Filled circles show the wind at 1-km intervals, and the unfilled circle shows the wind at 500 m.

c. Base-state substitution

The base state conditions of CM1 are horizontally homogeneous, which is beneficial for understanding the effects of different initializing environments on a storm. However, real storm environments rarely remain the same throughout a storm's lifetime, as the environment varies both spatially and temporally. Base-state substitution (BSS; Letkewicz et al. 2013) can be used to understand how a mature storm is modified by a changing environment. To apply BSS, the model simulation is paused and then restarted, preserving the perturbation fields while replacing the base state. Thus, thermodynamic and flow perturbations associated with the storm are preserved but the environment within which it is embedded changes. Typically this is done in a series of small increments ("gradual BSS") to avoid shocks to the model, although changes can also be applied with a single restart ("instantaneous BSS"). This technique has demonstrated its utility in several studies where the background wind and/or thermodynamic profiles have been varied (e.g., Coffer and Parker 2015; Davenport and Parker 2015). SB environments typically exhibit a gradual temperature gradient due to warming of the air mass as it moves inland (Robinson et al. 2013), although the wind changes are relatively sharp. However, it is reasonable to assume that the storm will take a finite amount of time to cross the SBF and, as will be shown, the results are not particularly sensitive to the duration of BSS. The CTRL simulation does not have an SB air mass introduced, with its base state environment unmodified as outlined by the sounding in Figs. 1a and 2. The remainder of the simulations, unless otherwise specified, have BSS applied gradually over a 15-min period initially utilizing a restart file produced by the CTRL simulation at $t = 75$ min. The simulation was restarted every 5 min during this period, with the new base state environment formed by linearly interpolating between the CTRL environment and the new environment. The duration of BSS was decided based

TABLE 1. Parameters that were used to define the thermodynamic profile in the CTRL simulation.

Definition (unit)	Value
Mixed-layer depth (km)	1.75
Potential temperature lapse rate in mixed layer (K km^{-1})	1
Pressure at mixed-layer top (hPa)	820
Temperature at mixed-layer top (K)	288
Relative humidity at mixed-layer top (%)	90
Tropopause height (km)	12
Relative humidity at tropopause (%)	25
Factor controlling relative humidity decrease	0.75
Surface-based CAPE (J kg^{-1})	1500
Height of max buoyancy (km)	7

TABLE 2. Thermodynamic and wind parameters for each simulated environment. Storm speed and direction are estimates, over the period t = 120–210 min, for each simulated storm computed using the Theil–Sen fit as in Lakshmanan et al. (2015).

	CTRL	SB1K	SB2K	WIND	TH1K	TH2K	WEAK	STRG
T_{sfc} (°C)	30.1	29.1	28.1	30.1	29.1	28.1	29.1	29.1
$T_{d,sfc}$ (°C)	17.2	19.2	19.2	17.2	19.2	19.2	19.2	19.2
Surface-based CAPE (J kg^{-1})	1500	2271	2024	1500	2271	2024	2271	2271
CIN (J kg^{-1})	49	52	80	49	52	80	52	52
LCL (m)	1641	1266	1141	1641	1266	1141	1266	1266
Subcloud layer-mean RH (%)	54.1	62.8	66.0	54.1	62.8	66.0	62.8	62.8
LFC (m)	2069	1697	1846	2069	1697	1846	1697	1697
Equilibrium level (m)	12 215	12 459	12 381	12 215	12 459	12 381	12 459	12 459
0–6-km bulk wind difference (m s^{-1})	15.5	19.3	19.3	19.3	15.5	15.5	17.3	21.4
Storm speed (m s^{-1})	8.3	6.7	7.1	6.9	8.3	8.6	7.6	7.2
Storm direction (°)	23.7	30.9	28.1	32.2	20.2	14.0	26.0	31.9
0–3-km SRH (m^2 s^{-2})	−45	−64	−61	−67	−40	−30	−51	−76

on the time taken for a storm to cross a boundary roughly perpendicular to its motion. The start time of t = 75 min was chosen as the initial storm began to show multicellular characteristics similar to the Brisbane hailstorm at this time.

Three primary simulations and nine sensitivity tests were performed, with two post-SB air masses being simulated using the BSS method. A summary of the ambient thermodynamic and wind profiles that were utilized for each experiment is provided in Table 4. The nine sensitivity tests are part of three broader groups of experiments. The first isolated the effect of the change in wind field (WIND) against the change in thermodynamic field (TH1K and TH2K for the modified and unmodified air masses, respectively). In the second test, the wind speed in the SB layer was reduced by 2.5 m s^{-1} (WEAK; Fig. 2c) or increased by 2.5 m s^{-1} (STRG; Fig. 2d), with the thermodynamic profile remaining the same as SB1K. In the third test, four experiments were conducted utilizing the SB1K thermodynamic and wind profiles to examine the effects of BSS timing. Here, either the time the SB air mass was introduced was changed, by starting BSS at t = 60 min (EARL) or t = 90 min (LATE), or the length of time that it took to introduce the air mass was changed, where BSS was applied either instantaneously (INST) or over a 30-min period (LONG).

3. Results

Figure 3 shows the evolution of the CTRL simulation from t = 60–90 min. The initial warm bubble triggers an isolated convective cell that splits into left- and right- moving storms. At t = 60 min, the right-moving cell features some supercellular characteristics including a strong reflectivity gradient and a pronounced inflow notch on the southern side of the storm. However, it is already outflow dominant at this time and rapidly decays over the subsequent 30 min. In contrast, the left-moving storm maintains moderate strength updrafts toward the rear flank while weaker updrafts form within the forward flank, leaving it with clear multicell characteristics by t = 90 min.

The following analysis is divided into four sections and focuses on the left-moving storm after BSS is applied. In the first section, the CTRL simulation and those simulations where the SB air masses are introduced at t = 75 min are considered (SB1K and SB2K). In the second section, the simulations where only the thermodynamic or wind profile was changed are considered (WIND, TH1K, and TH2K). Sensitivity to wind speed is analyzed in the third section (WEAK and STRG), while the final section considers those simulations where BSS timing or duration is changed (EARL, LATE, INST, and LONG).

To track the storm as it evolves, a moving analysis domain is used with the midpoint defined as the centroid of data points where midlevel ($z \approx 5$ km) vertical velocity is above 5 m s^{-1}. Where no points meet these criteria, the centroid of reflectivity values above 40 dBZ is used instead. This occurs toward the end of a few simulations (CTRL and TH2K) in which the storm eventually decays. The updraft centroid locations of each storm are stored to calculate individual storm motion over the period t = 120–210 min using the Theil–Sen fit as in Lakshmanan et al. (2015). This is used in the calculation of 0–3-km SRH in Table 2 and storm relative flow, which is calculated by first subtracting storm motion from the u- and v-components of wind and converting this to the along-section component of wind. Various aspects of storm intensity are summarized in Table 5

TABLE 3. Wind speed and direction at different heights used to define the wind profile of the control (CTRL), SB (SB1K, SB2K), WEAK, and STRG simulations.

	CTRL		SB1K, SB2K		WEAK		STRG	
Height (m)	Speed (m s^{-1})	Direction (°)	Speed (m s^{-1})	Direction (°)	Speed (m s^{-1})	Direction (°)	Speed (m s^{-1})	Direction (°)
0	5	202.5	7.5	225	5	225	10	225
500	—	—	5	225	2.5	225	7.5	225
1000	5	135	5	135	5	135	5	135
3000	7.5	90	7.5	90	7.5	90	7.5	90
12 000	30	90	30	90	30	90	30	90

TABLE 4. Summary of the simulations conducted stating the relevant panel of Fig. 1 that describes the thermodynamic environment (second column), the relevant panel of Fig. 2 that describes the winds in the 0–6-km layer (third column), the start time of BSS (fourth column), and the end time of BSS (final column).

Simulations	Thermodynamic profile	Wind profile	BSS start time	BSS end time
CTRL	Fig. 1a	Fig. 2a	—	—
SB1K	Fig. 1b	Fig. 2b	75	90
SB2K	Fig. 1c	Fig. 2b	75	90
WIND	Fig. 1a	Fig. 2b	75	90
TH1K	Fig. 1b	Fig. 2a	75	90
TH2K	Fig. 1c	Fig. 2a	75	90
WEAK	Fig. 1b	Fig. 2c	75	90
STRG	Fig. 1b	Fig. 2d	75	90
EARL	Fig. 1b	Fig. 2b	60	75
LATE	Fig. 1b	Fig. 2b	90	105
INST	Fig. 1b	Fig. 2b	75	75
LONG	Fig. 1b	Fig. 2b	75	105

using swath diagnostics from the end of each simulation, restricted to the portion of the domain containing the left-moving storm after BSS ($100 \le x \le 180$ km and $90 \le y \le 170$ km). These diagnostics represent the maximum/minimum of a particular variable at every grid point computed across all model time steps. Here we consider the area and area-mean value of the following quantities: minimum 2–5-km updraft helicity $\le -100\,\mathrm{m^2\,s^{-2}}$ (Kain et al. 2008), maximum 5-km vertical velocity $\ge 10\,\mathrm{m\,s^{-1}}$, maximum surface hail mixing ratio $\ge 0.25\,\mathrm{g\,kg^{-1}}$, and maximum surface wind speeds $\ge 15\,\mathrm{m\,s^{-1}}$ for all experiments. In addition to absolute values, Table 5 also gives the percentage difference with respect to the CTRL simulation.

a. Sea-breeze experiments

Figure 4 provides a comparison of the CTRL, SB1K, and SB2K simulations from $t = 120$ min until the end of the simulation period ($t = 210$ min). Characteristics of the storms are summarized by the swath plots of Fig. 5 and time series of Fig. 6. Vertical cross sections through the midlevel updraft centroid, along the angle of storm motion, are displayed in Fig. 7 to gain a more detailed understanding of storm characteristics near the cold-pool boundary. Figure 8 displays time-averaged vertical profiles of the area, mean buoyancy, mean velocity and mean vorticity of updrafts (defined as points with $w \ge 5\,\mathrm{m\,s^{-1}}$) averaged over the period $t = 120$–180 min. Buoyancy is defined here as

$$B = g\frac{\theta_\rho - \theta_{\rho 0}}{\theta_{\rho 0}},$$

where g is the acceleration due to gravity, θ_ρ is the density potential temperature, and $\theta_{\rho 0}$ is the base-state density potential temperature (Bryan 2017). These profiles are calculated by taking a 20×20–km^2 box around the midlevel updraft

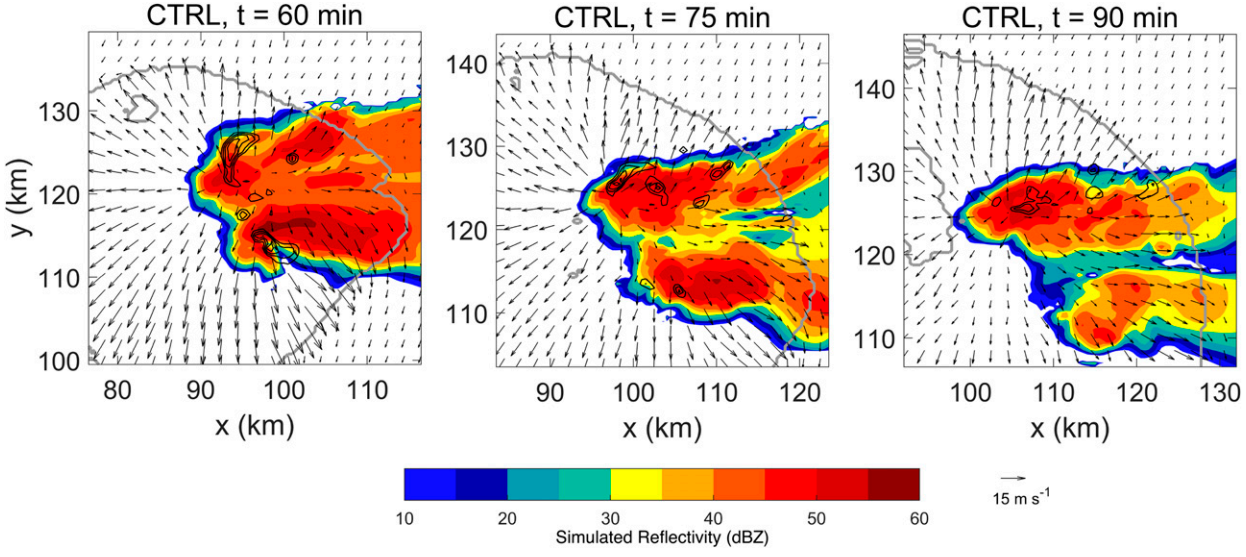

FIG. 3. Evolution of the CTRL storm for $t = 60$–90 min in 15-min increments. Variables shown are lowest-model-level ($z = 25$ m) reflectivity (filled contours; dBZ), cold-pool boundary (thick gray contour $\theta' = -1$ K), and ground-relative winds (vectors; reference vector is next to the color bar) and midlevel ($z \approx 5$ km) vertical velocity (thin black contours, every $5\,\mathrm{m\,s^{-1}}$ starting at $5\,\mathrm{m\,s^{-1}}$).

TABLE 5. Mean value and total area of minimum 2–5-km updraft helicity swath $\leq -100\,m^2\,s^{-2}$, maximum 5-km vertical velocity swath $\geq 10\,m\,s^{-1}$, maximum surface hail mixing ratio swath $\geq 0.25\,g\,kg^{-1}$, and maximum surface wind speed swath $\geq 15\,m\,s^{-1}$ for each simulation over the domain $100 \leq x \leq 180$ km, $90 \leq y \leq 170$ km; numbers in parentheses give the percentage change of the absolute magnitude of each field relative to the CTRL storm.

	CTRL	SB1K	SB2K	WIND	TH1K	TH2K	WEAK	STRG	INST	LONG	EARL	LATE
Helicity swath mean ($m^2\,s^{-2}$)	−192	−231	−222	−228	−211	−204	−205	−246	−248	−220	−243	−231
		(20)	(16)	(19)	(10)	(6)	(7)	(28)	(29)	(15)	(27)	(20)
Helicity swath area (km^2)	283.50	377.25	393.00	379.50	295.75	208.00	286.00	507.00	439.50	372.50	488.00	363.50
		(33)	(39)	(34)	(4)	(−27)	(1)	(79)	(55)	(31)	(72)	(28)
Updraft swath mean ($m\,s^{-1}$)	16.0	16.9	16.4	16.7	16.5	16.0	16.2	17.2	16.9	16.7	17.3	16.5
		(6)	(3)	(4)	(3)	(0)	(1)	(8)	(7)	(4)	(8)	(3)
Updraft swath area (km^2)	518.50	599.50	632.50	609.75	491.50	362.00	509.50	721.75	649.75	605.75	738.25	597.00
		(16)	(22)	(18)	(−5)	(−30)	(−2)	(39)	(25)	(17)	(42)	(15)
Hail swath mean ($g\,kg^{-1}$)	0.28	0.33	0.34	0.31	0.28	0.27	0.31	0.31	0.28	0.29	0.29	0.3
		(18)	(21)	(11)	(0)	(−4)	(11)	(11)	(0)	(4)	(4)	(7)
Hail swath area (km^2)	17.00	53.50	44.00	47.00	25.25	10.00	28.75	79.00	27.50	36.00	22.00	29.75
		(215)	(159)	(176)	(49)	(−41)	(69)	(365)	(62)	(112)	(29)	(75)
Wind swath mean ($m\,s^{-1}$)	19.1	18.9	18.9	19.3	19.2	19.3	18.8	20.1	19.8	18.6	20.2	18.8
		(−1)	(−1)	(1)	(1)	(1)	(−2)	(5)	(4)	(−3)	(6)	(−2)
Wind swath area (km^2)	2593.25	1955.00	1297.25	2547.75	2341.75	1131.00	1614.25	3254.50	3340.75	1891.00	3978.75	1690.50
		(−25)	(−50)	(−2)	(−10)	(−56)	(−38)	(25)	(29)	(−27)	(53)	(−35)

centroid and calculating updraft characteristics at each height and each output time step. The average of these characteristics is then taken over the time period specified.

At $t = 120$ min, the midlevel updraft of all three storms is located near the outflow boundary (Fig. 4, top row), placing it in a position where it can ingest potentially buoyant air from the warm side of the boundary. However, by $t = 150$ min, the cold pool of the CTRL storm has surged ahead of its midlevel updraft due to weak low-level environmental winds opposing gust-front motion (Figs. 4 and 7). In contrast, the low-level environmental winds in the SB simulations are stronger and more orthogonal to the gust front, which slows progression ahead of the main updraft (Fig. 7). In addition, the outflow of the CTRL storm is more intense than that of the SB storms, as depicted by the low-level wind vectors of Fig. 4, the maximum surface wind swath of Figs. 5j–l and the storm-relative flow in Fig. 7. This stronger outflow further assists the CTRL cold-pool propagation away from the midlevel updraft, resulting in separation between the low-level and midlevel updrafts and storm decay beginning at $t \approx 195$ min (Figs. 6a and 7). Meanwhile, slowed gust-front progression causes the low-level updraft of both SB storms to remain connected to the midlevel updraft, allowing the SB storms to persist until the end of the simulation.

From $t \approx 135$ min, both SB storms have a stronger midlevel updraft than the CTRL storm (Figs. 5d–f and 6a). Above approximately 3 km, average updraft buoyancy is larger in the SB storms than the CTRL storm (Fig. 8b). The air parcels within the SB air mass have larger surface-based CAPE than those in the CTRL environment (increase by 771 and 524 $J\,kg^{-1}$ for SB1K and SB2K, respectively; Table 2), and so maintaining inflow from within the SB air mass would be beneficial to the storm. The increased buoyancy in the SB storms suggests that inflow from within the SB air mass is being maintained, and would be the primary contributor to the heightened updraft strength. Soderholm et al. (2017b) proposed that inflow parcels sourced from the SB air mass contributed to increased updraft strength and that these parcels were lifted to their LFC as the cold pool of the storm was cooler than the SB air mass, creating a stronger baroclinically generated circulation forcing the SB air above the cold pool. However, here we propose that the mechanism may be in part due to the increase in low-level storm-relative inflow causing the gust front to slow, and greater low-level convergence leading to a more connected low-level and midlevel updraft (Fig. 7). The associated increase in updraft strength and area (velocity and area at 7 km approximately 10.5 $m\,s^{-1}$ and 25 km^2 for CTRL, respectively, compared to 12.4 $m\,s^{-1}$ and 35 km^2 for SB2K, and 12.6 $m\,s^{-1}$ and 40 km^2 for SB1K; Fig. 8) for both SB storms results in an increase in the total condensate mass compared to the CTRL storm (Fig. 6c). Further, there is an increase in the area and intensity of the maximum surface hail swath for the SB storms compared to the CTRL with an additional increase in the hail swath area in SB1K compared to SB2K, presumably due to the greater updraft area of SB1K (hail swath area of 53.5 km^2 for SB1K as compared with 44.0 km^2 for SB2K and 17.0 km^2 for CTRL; Table 5 and Figs. 5g–i).

Previous studies suggest the SBF is necessary for storms to develop increased updraft rotation (e.g., Soderholm et al. 2017b);

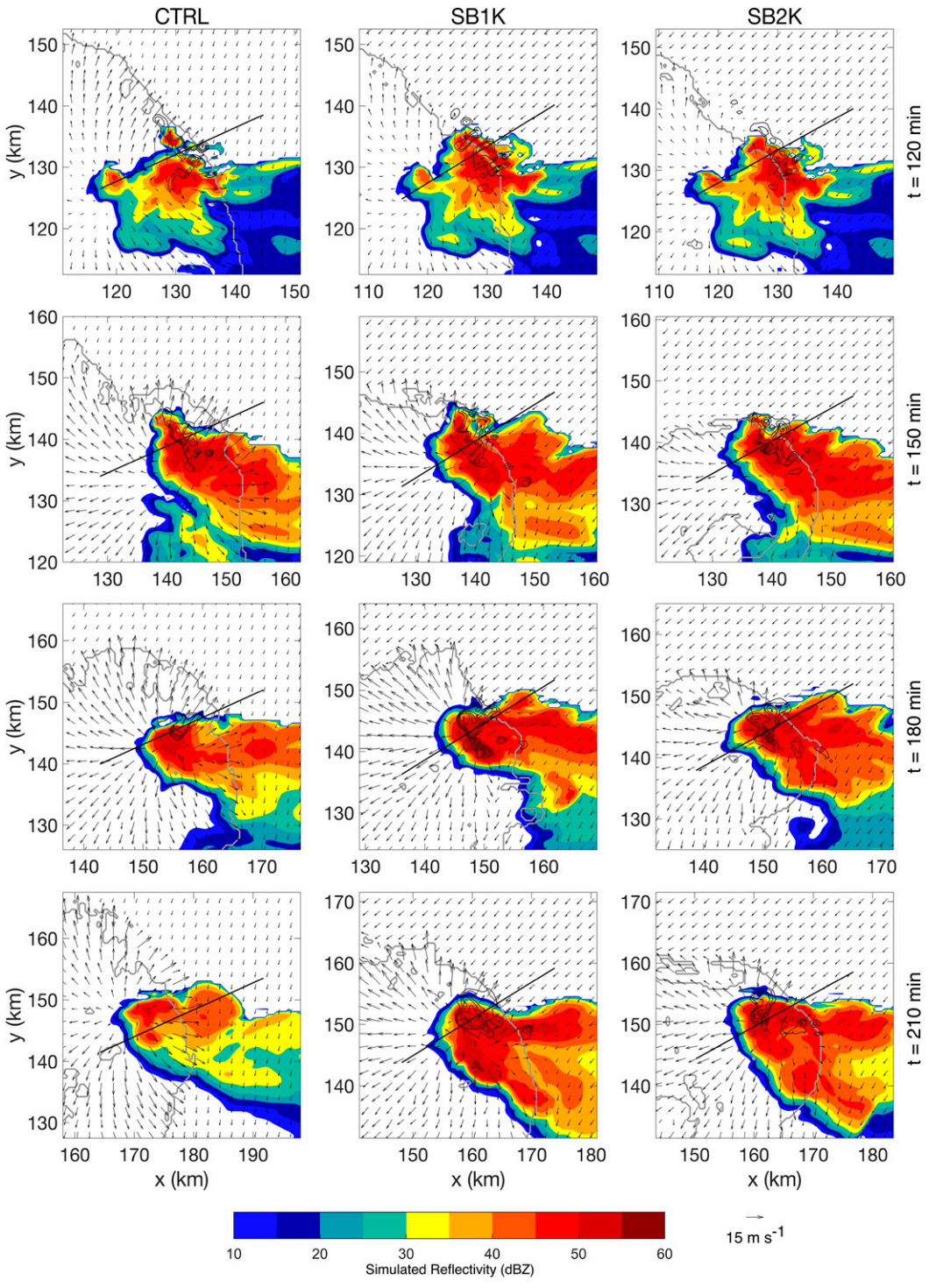

FIG. 4. Evolution of (left) CTRL, (middle) SB1K, and (right) SB2K storms at 30-min increments, beginning at (top) $t = 120$ min and ending at (bottom) $t = 210$ min. Variables shown are as in Fig. 3. The thin black line denotes the location and extent of the vertical cross sections in Fig. 7, below.

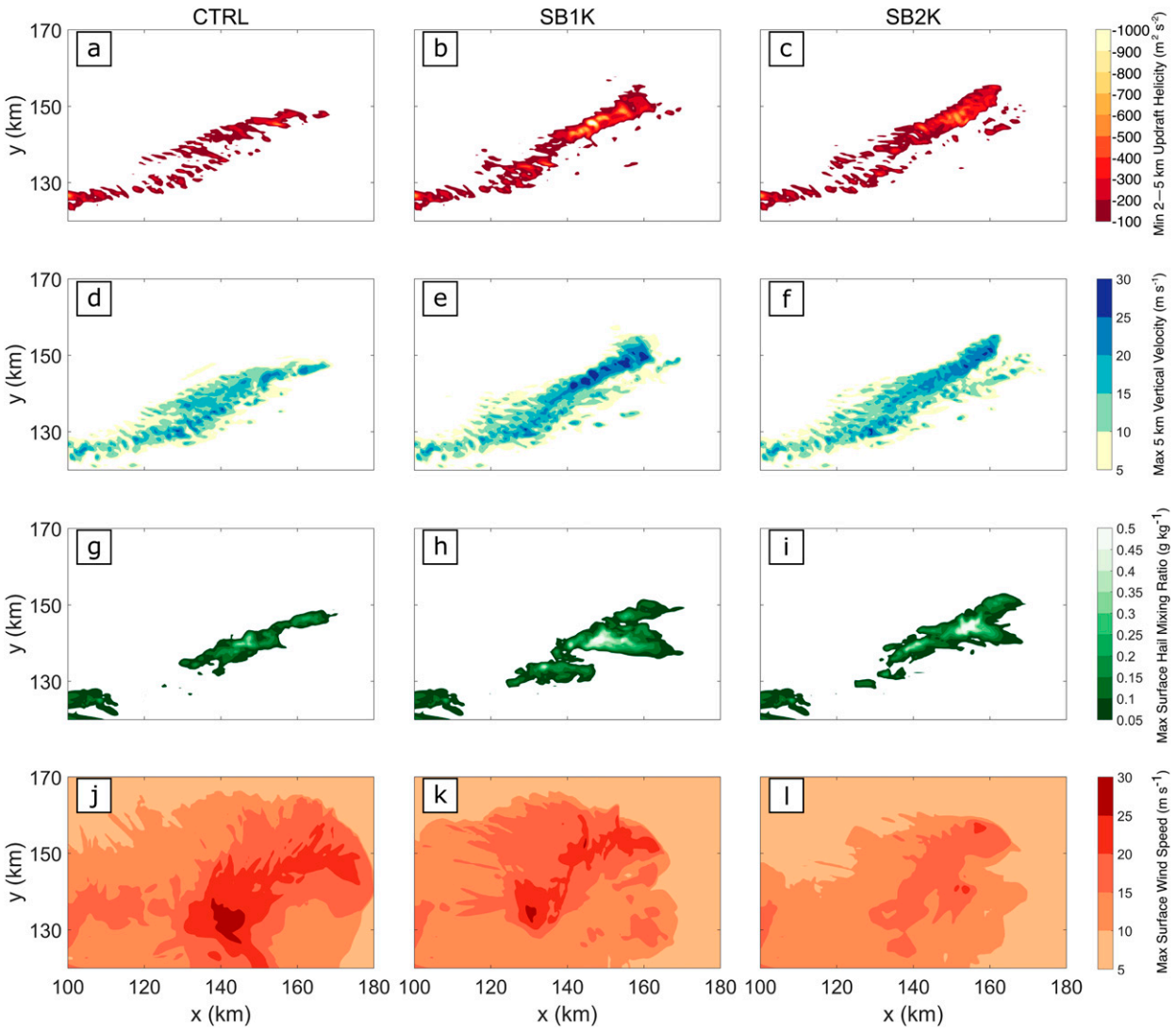

FIG. 5. Swath variables for the (left) CTRL, (middle) SB1K, and (right) SB2K simulations showing (a)–(c) minimum 2–5-km updraft helicity, (d)–(f) maximum vertical velocity at $z = 5$ km, (g)–(i) maximum surface hail mixing ratio, and (j)–(l) maximum surface wind speed. The domain is restricted to focus on the left-moving storm during the period after BSS ($t = 90$–210 min).

however, the SB storms develop increased rotation within their updraft relative to the CTRL storm, despite the lack of a simulated SBF. Figure 5a shows a more pronounced negative updraft helicity swath in both SB simulations, but especially SB1K, compared to CTRL. The area with updraft helicity $\leq -100\,\mathrm{m^2\,s^{-2}}$ increases from 283.5 km^2 in CTRL to 393.0 km^2 in SB2K and 377.25 km^2 in SB1K (Table 5). While the increase in updraft helicity in part reflects the stronger updrafts in the SB storms, there is also an increase in the magnitude of updraft vorticity in the majority of the SB storm updrafts when averaged over $t = 120$–180 min (Fig. 8d), particularly at low-levels and mid- to upper levels of the updraft (Fig. 6b). The strengthened vorticity is consistent with the increased BWD to 19.3 m s^{-1} (Table 2), which is sufficient for supercell convection (Weisman and Klemp 1982, 1984; Bunkers 2002; Houston et al. 2008). Similar to Richardson et al. (2007), this increase in BWD appears sufficient for both SB storms to become increasingly organized and display characteristics consistent with supercell convection. While the vorticity magnitude falls below the 0.01 s^{-1} threshold used to define mesocyclones in some previous studies (e.g., Trapp et al. 2017), updraft rotation is clearly persistent in both SB storms (Figs. 5b,c). Furthermore, toward the end of the simulations, both SB storms show clear supercell characteristics, including a v-notch feature and sharp reflectivity gradients (Fig. 4) and motion to the left of the mean wind vector (Fig. 5).

It might be expected for the maximum surface wind speeds in the SB simulations to be larger than the CTRL storm, as a result of the higher total condensate mass and therefore greater hydrometeor loading and stronger latent cooling through evaporation, melting, and sublimation of falling precipitation. However, the surface winds associated with the

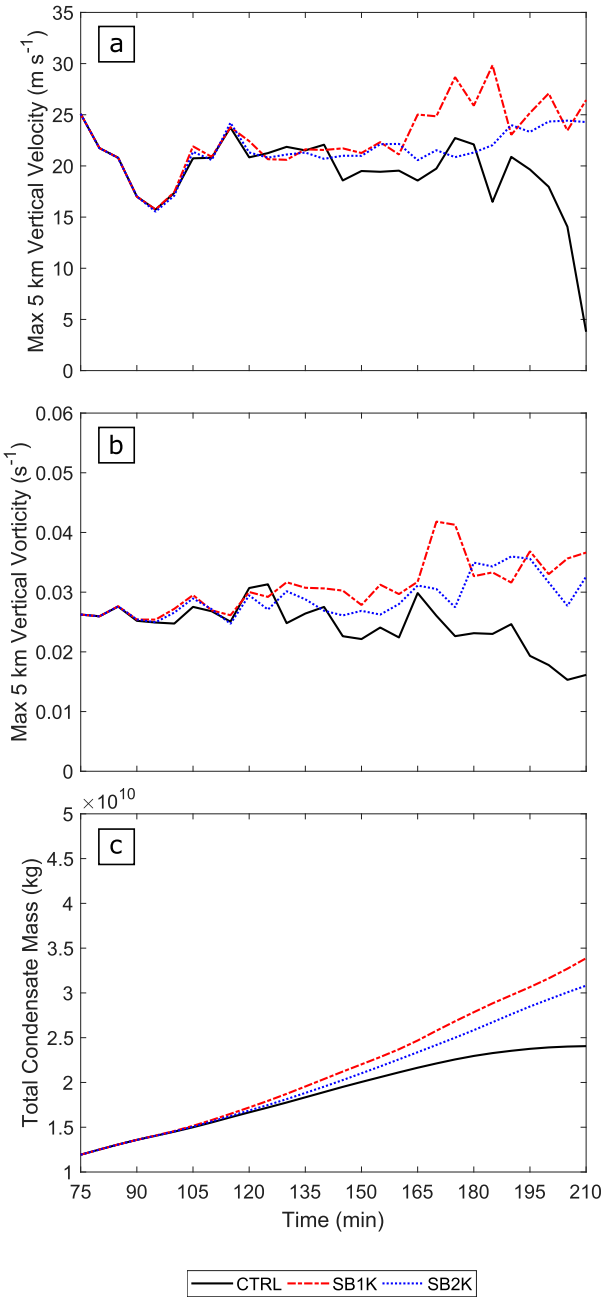

FIG. 6. Time series for the CTRL (black), SB1K (red), and SB2K (blue) simulations for $t = 75$–210 min showing (a) maximum 5-km vertical velocity, (b) maximum 5-km vertical vorticity, and (c) total condensate mass.

CTRL storm show a larger area of winds between 25 and 30 m s^{-1} relative to the SB1K storm, whereas the SB2K storm has no such values after the beginning of the BSS period (Fig. 5). The LCL in the CTRL environment is much higher than both SB environments (1641 m versus 1266 and 1141 m; Table 2) corresponding to the reduction in dewpoint temperature in the lowest 500 m of the CTRL environment by 2 K. Therefore, the increased surface winds in the CTRL storm are likely due to the subcloud air being significantly drier and deeper than that of the SB air masses (RH of 54.1% for CTRL as compared with 62.8% for SB1K and 66.0% for SB2K; Table 2, Figs. 1 and 7), leading to more evaporative cooling.

These results found increased storm longevity and organization in both SB storms due to the change in the background environment. The SB storms were more intense than the CTRL storm, with a further increase in intensity for the storm in the warmed SB air mass, due to greater buoyancy in the environment, although it displayed similar morphological traits to the storm that developed in the unmodified SB air mass.

b. *Relative role of thermodynamic and wind changes*

Three experiments were conducted varying only the thermodynamic or wind profiles to assess the relative contributions of the thermodynamic and wind profile changes to storm longevity and intensity. These simulations are summarized by plots of storm structure in Fig. 9 and the time series plots in Fig. 10. Upon comparison with the CTRL, SB1K, and SB2K simulations, it is evident that only the WIND storm maintains a relatively long life, while both TH1K and TH2K storms dissipate before the simulation has completed (Figs. 9 and 10). This demonstrates that the change in the low-level wind field within the SB air mass is the primary factor responsible for both storm intensification and longevity within the simulations. While the warmer air mass permits the storm within TH1K to outlive the storm within TH2K (Fig. 10a), the presence of a more favorable thermodynamic environment is alone insufficient in supporting the storms throughout the simulation period. Having flow that is orthogonal to and opposing the gust front of a storm can slow its progression, preventing it from undercutting the updraft. As there have been no changes to other environmental variables relative to CTRL, this slowing of gust-front progression appears essential to the increase in storm longevity for the WIND storm.

The increased CAPE in the TH1K environment makes little difference to storm longevity relative to the CTRL (Fig. 10). Meanwhile, the TH2K storm begins to dissipate around $t \approx 165$ min, which is significantly earlier than the CTRL storm. While there has been an increase in CAPE in the TH2K run, there has also been a substantial increase in CIN (Table 2). This increase in CIN requires stronger dynamical forcing for it to be overcome and the additional CAPE in the SB air mass to be realized. At $t = 210$ min, TH2K appears elevated because there is still a reflectivity signal, yet there is no clear gust front, and the surface winds appear to be undisturbed (Fig. 9). However, the reflectivity signal is just a remnant of the decayed storm as there is no updraft at this point in time (not shown) and precipitation continues to fall out or evaporate. This demonstrates how the lack of change in the low-level environmental winds do not promote lifting along the gust front and allow the outflow to overwhelm the weak inflow, leading to rapid storm decay (Fig. 10a).

The WIND simulation has similar maximum 5-km vertical vorticity as the SB1K and SB2K runs (Figs. 6b and 10b). As in Richardson et al. (2007), the increase in low-level shear appears sufficient for the WIND storm to become more organized, with the storm displaying characteristics commonly observed in supercells including a v-notch feature, sharp

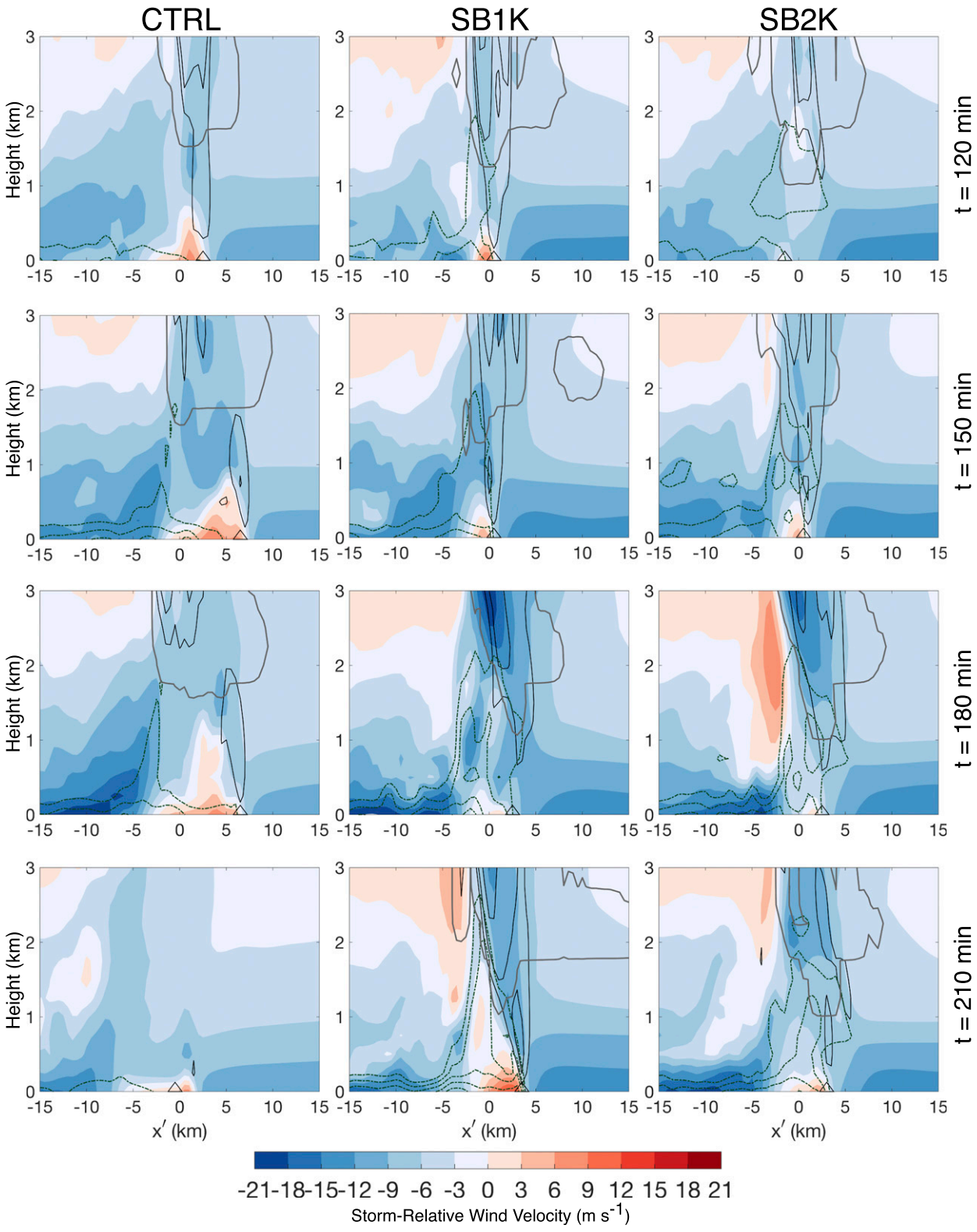

FIG. 7. Vertical cross sections for the (left) CTRL, (middle) SB1K, and (right) SB2K simulations displaying storm-relative flow (filled contours), cloud water content (thick gray contour = 0.01 g kg^{-1}), vertical velocity (thin black contours; at 2.5, 5, 10, and 20 m s^{-1}), negative buoyancy (green dashed contours every −0.05 m s^{-2}, starting at −0.05 m s^{-2}), and the leading edge of the cold pool (triangle, where $\theta' = -1$ K), beginning at (top) $t = 120$ min and ending at (bottom) $t = 210$ min. Cross sections are taken through the midlevel updraft centroid at that time step, parallel to the average storm motion vector, as depicted in Fig. 4.

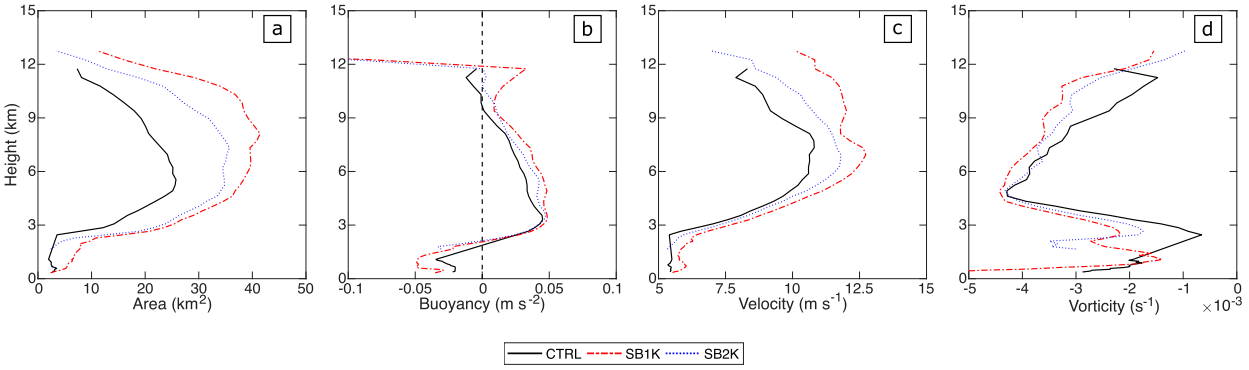

FIG. 8. Time-averaged (t = 120–180 min) vertical profiles of the (a) area, (b) mean buoyancy, (c) mean vertical velocity, and (d) mean vorticity of updrafts ($w \geq 5$ m s^{-1}) for the CTRL (black), SB1K (red), and SB2K (blue) storms. There is a sudden drop in buoyancy after 12 km in (b), likely because of masking by gravity waves in this layer and resulting values being less than the minimum value on the axis. Levels at which there are fewer than seven output times with at least four updraft points are masked.

reflectivity gradient, deviation to the left of the mean wind vector and stronger updraft rotation (Fig. 9 and Table 5). Meanwhile, both the TH1K and TH2K storms display characteristics consistent with multicellular convection until they are undercut by their cold pools and decay (not shown).

The WIND storm has greater updraft strength and area compared to the CTRL (4% in mean updraft strength and 18% in updraft area; Table 5 and Fig. 10a), resulting in significantly larger total condensate mass than the CTRL storm (Fig. 10c). There is also a corresponding increase in the mean surface hail

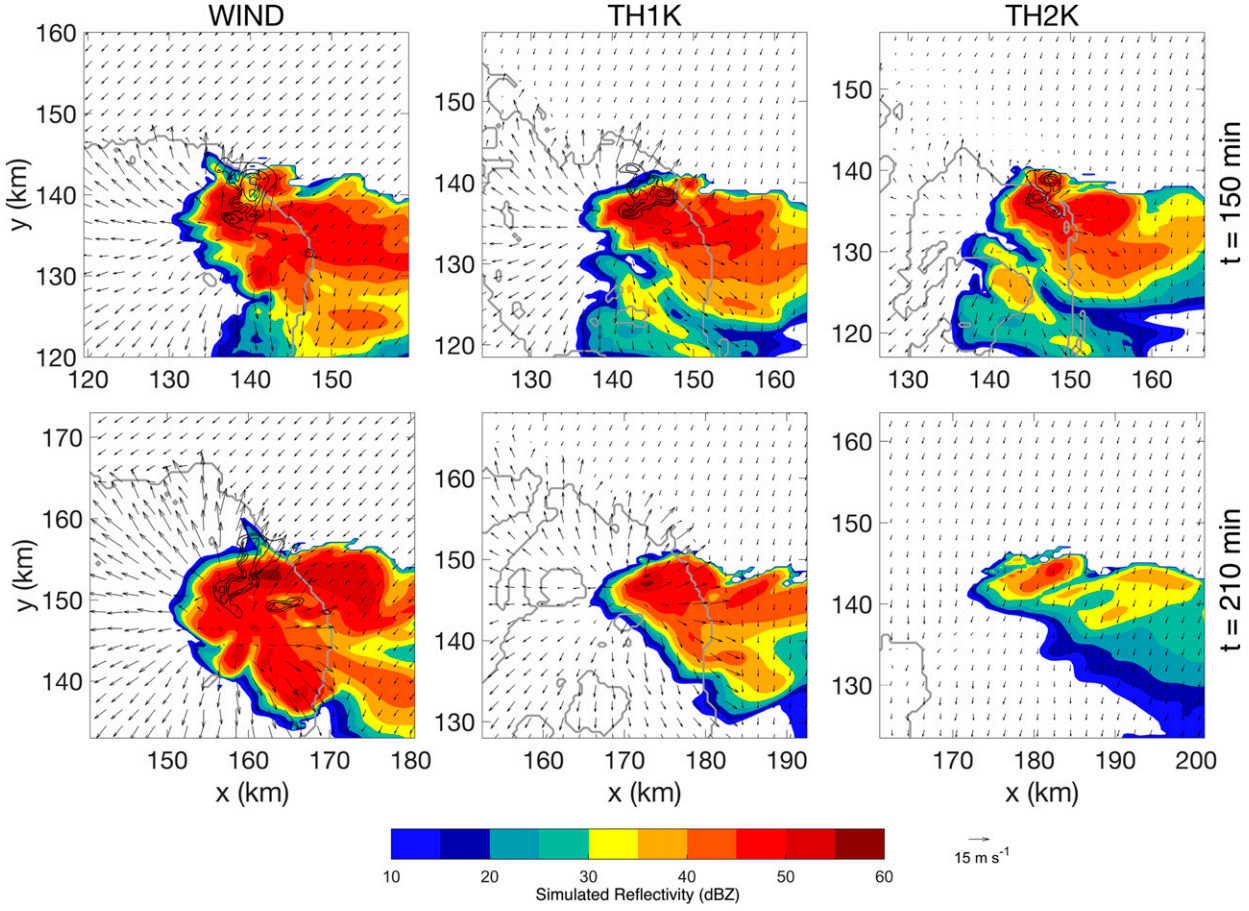

FIG. 9. Storm structure at (top) t = 150 min and (bottom) t = 210 min for the (left) WIND, (center) TH1K, and (right) TH2K storms. Variables shown are as in Fig. 3.

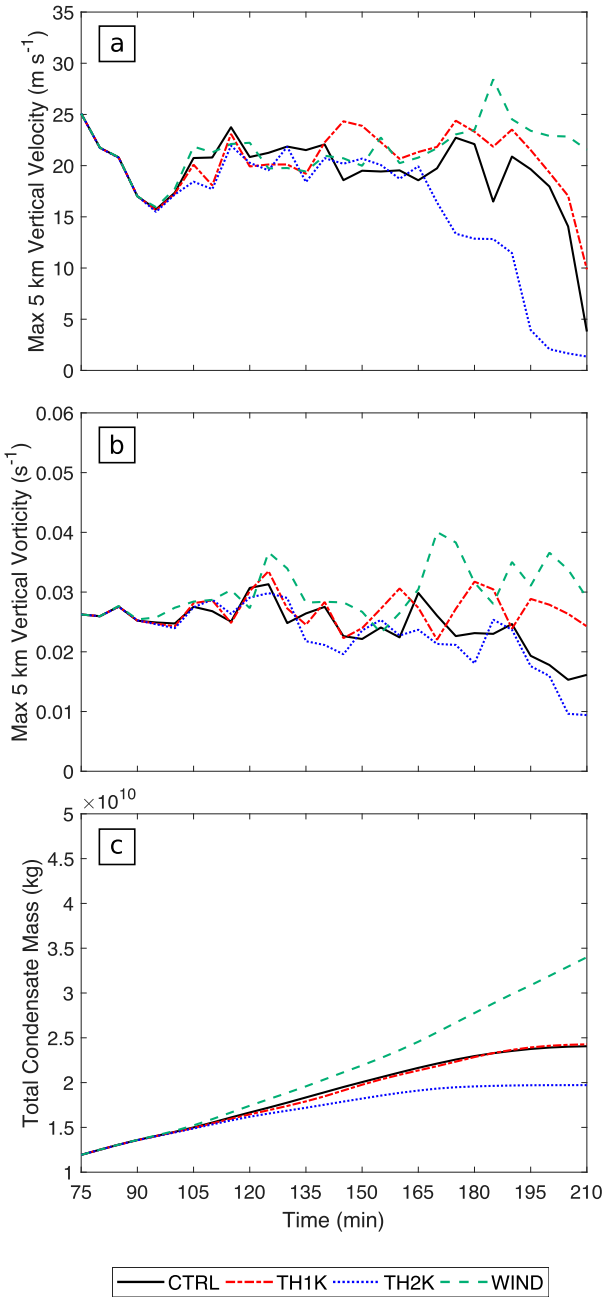

FIG. 10. As in Fig. 6, but for the WIND (green), SB1K (black), TH1K (red), and TH2K (blue) simulations.

mixing ratio by 11% and more than a doubling of the swath area (Table 5). For TH1K and TH2K, there are little changes to storm intensity compared to the CTRL, with negligible changes to mean swath values except for an increase in helicity swath means (increase compared to the CTRL of 10% for TH1K and 6% for TH2K, Table 5). There are more noticeable changes to the swath area, with decreases in the majority of variables compared to the CTRL for TH2K (e.g., a decrease of 56% in wind swath area) and a mixture of increases (e.g., 49% in hail swath area) and decreases (e.g., 10% in wind swath area) for TH1K (Table 5). It might be expected that the increased subcloud moisture in the TH1K and TH2K environments could lead to weaker mean surface wind speeds due in part to reduced evaporative cooling, but this does not occur with mean surface wind swath speeds slightly increasing by approximately 1% for both simulations (Table 5).

These experiments, varying only the kinematic or thermodynamic environment, highlight the importance of the changes in the low-level wind field to increased storm longevity and intensity. Without the kinematic changes, the storm continues to decay or, as in the case of the cooler thermodynamic environment, the storm decays earlier than the CTRL. However, when the low-level wind field is more orthogonal to and opposing the storm gust front, the gust front is constrained, leading to a longer-lived storm. The changes to the environmental winds also result in a stronger, more organized storm.

c. *Sensitivity to sea-breeze wind strength*

The winds within SB air masses vary in strength depending on the temperature gradient between the ocean and land surface, location within the air mass, and the strength and direction of the cross-shore component of the ambient wind (Miller et al. 2003). In this section, we address the question of how much the varied SB wind strength affects storm longevity and structure by utilizing the thermodynamic and wind profiles of SB1K and either reducing wind speed in the 0–500 m layer by 2.5 m s^{-1} (WEAK; Fig. 2c and Table 4) or increasing wind speed by 2.5 m s^{-1} (STRG; Fig. 2d and Table 4). The effect of SB strength on storm longevity is summarized by the storm snapshot taken at $t = 210$ min in Fig. 11, and the time series in Fig. 12.

The maximum midlevel vertical velocity of the WEAK run begins to decrease around $t \approx 180$ min, signaling the storm's demise (Fig. 12a). Upon comparison with the CTRL simulation (Fig. 6a), there is an increase in longevity of the WEAK storm. This would be partly due to the change in thermodynamic characteristics, which caused an increase in lifetime of the TH1K storm. However, the WEAK storm maintains a midlevel updraft to the end of the simulation while the TH1K storm does not (Figs. 9 and 11). This suggests that the additional change in low-level environmental winds to a northeasterly direction, with no concurrent increase in wind speed, is sufficient for a minor increase in the lifetime of the simulated storm. The environmental winds are more orthogonal to the gust front of the WEAK storm, slowing its progression (Fig. 11). This allows the storm to continue to ingest potentially buoyant air ahead of the cold pool. However, as the low-level inflow is relatively weak, it is eventually overwhelmed by the storm's outflow and the WEAK storm begins to decay toward the end of the simulation (Fig. 12a). Alternatively, low-level environmental flow is stronger in the STRG simulation. This slows gust-front progression and is strong enough for sufficient low-level inflow feeding the storm (not shown), allowing it to persist to the end of the simulation period, much like the SB1K storm.

The WEAK storm maintains a multicell structure (Fig. 11), with a 7% increase in intensity of the 2–5-km updraft helicity

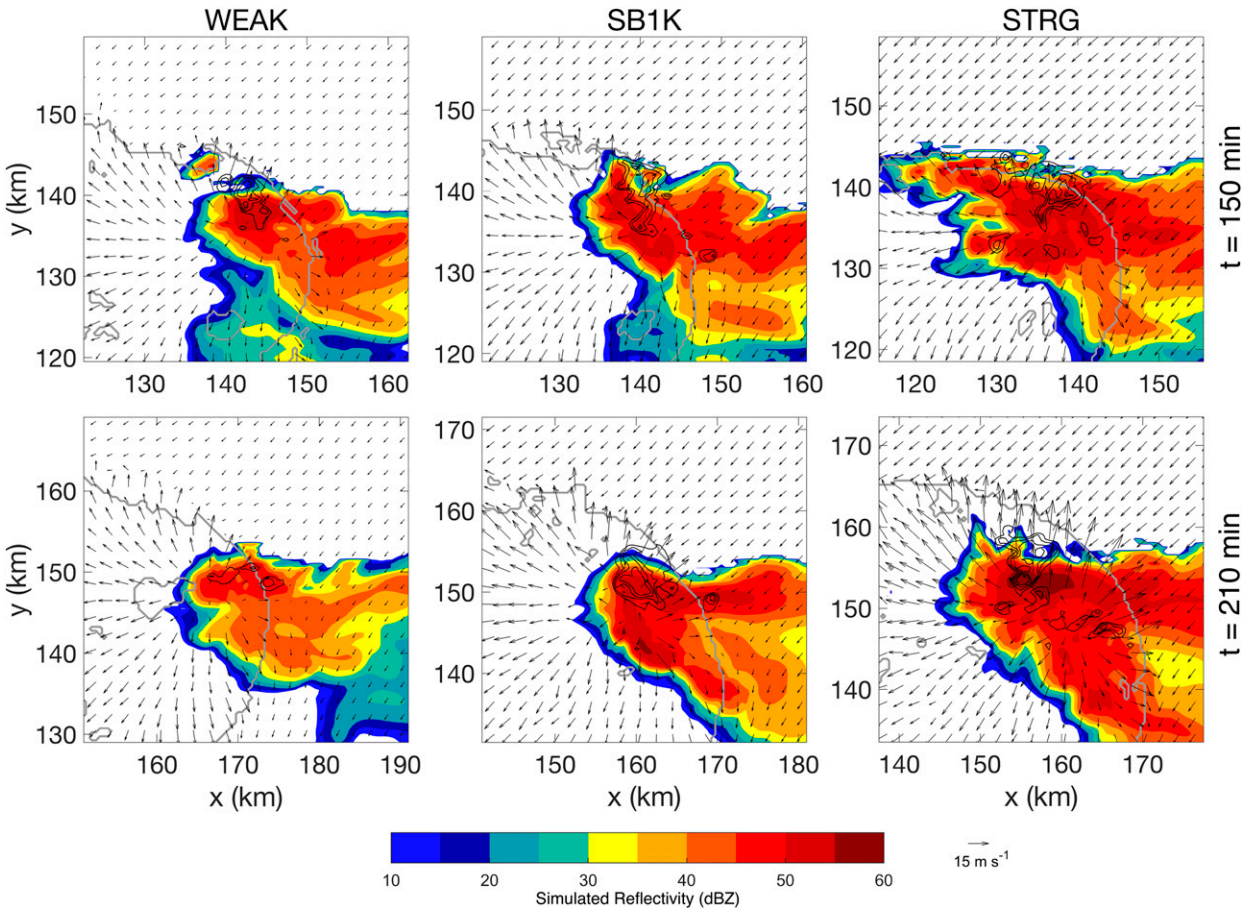

FIG. 11. As in Fig. 9, for the (left) WEAK, (center) SB1K, and (right) STRG storms.

compared to the CTRL storm, but only an increase in the area from 283.5 to 286.0 km^2 (Table 5). The increase in low-level shear and resulting 0–3-km SRH in the STRG environment ($-76\,m^2\,s^{-1}$) relative to SB1K ($-64\,m^2\,s^{-1}$; Table 2) favors increased updraft rotation (increase in mean magnitude of helicity of approximately 6% and helicity swath area of 34%; Table 5 and Fig. 12b). Further, enhanced low-level inflow leads to a wider, more intense updraft (721.75 km^2 for STRG compared to 599.50 km^2 for SB1K, increase in updraft swath mean by 2%; Table 5) while multiple smaller updrafts are located within the storm and near the gust front (Fig. 11). This promotes enhanced total condensate mass (Fig. 12c) and stronger outflow compared to the SB1K storm (6% increase in wind swath mean, Table 5). While the low-level inflow slows gust-front propagation and supports regeneration of deep updrafts, the enhanced outflow of the STRG storm eventually overcomes the strong low-level inflow toward the end of the simulation. This causes the gust front to begin to surge ahead of the STRG storm (Fig. 11), leading to a separation of the low- and midlevel updrafts (not shown); however, it is unknown whether this would ultimately lead to the storm's demise since longer simulations were not performed.

The results show that there is sensitivity to the strength of the low-level environmental winds as this influences how well the gust front can be constrained near the updraft, and the connection between low- and midlevel updrafts. It is evident that the change in low-level shear orientation to be more orthogonal to the gust front of a storm might slightly increase storm longevity as it briefly constrains the gust front. However, the increase in low-level shear working in tandem with the change in direction results in a significantly longer lifetime and a larger, more intense storm.

d. Sensitivity to BSS timing and duration

All of the simulations considered in the previous sections introduced the thermodynamic and/or kinematic changes 75 min into the simulation, with a transition period to the new background environment of 15 min. The initial storm is not in a steady state, as can be seen from its eventual demise in the CTRL simulation (Fig. 4), thus its response to the SB air mass is likely to depend on the timing and duration of the BSS procedure. To assess this sensitivity, four additional simulations were performed with either BSS timing (EARL, LATE) or BSS duration (INST, LONG) modified (Table 4). These results are summarized in the time series plots in Fig. 13.

It is immediately discernable that there is no significant change in storm lifetime compared to the SB1K storm when

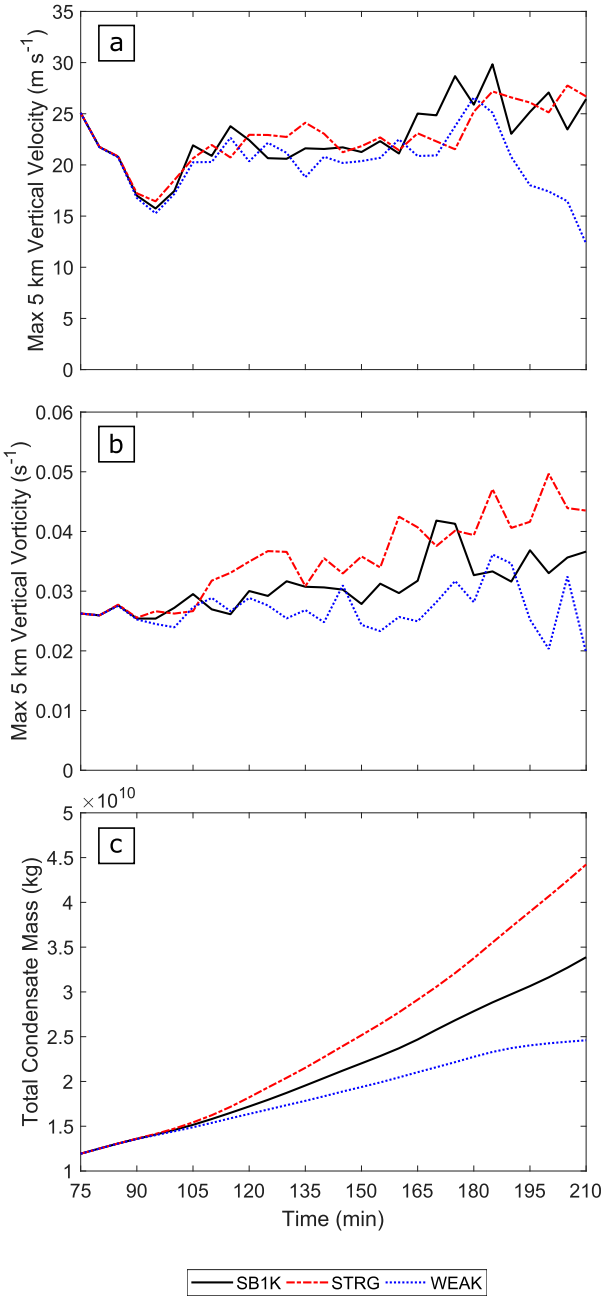

FIG. 12. As in Fig. 6, but for the SB1K (black), STRG (red), and WEAK (blue) simulations.

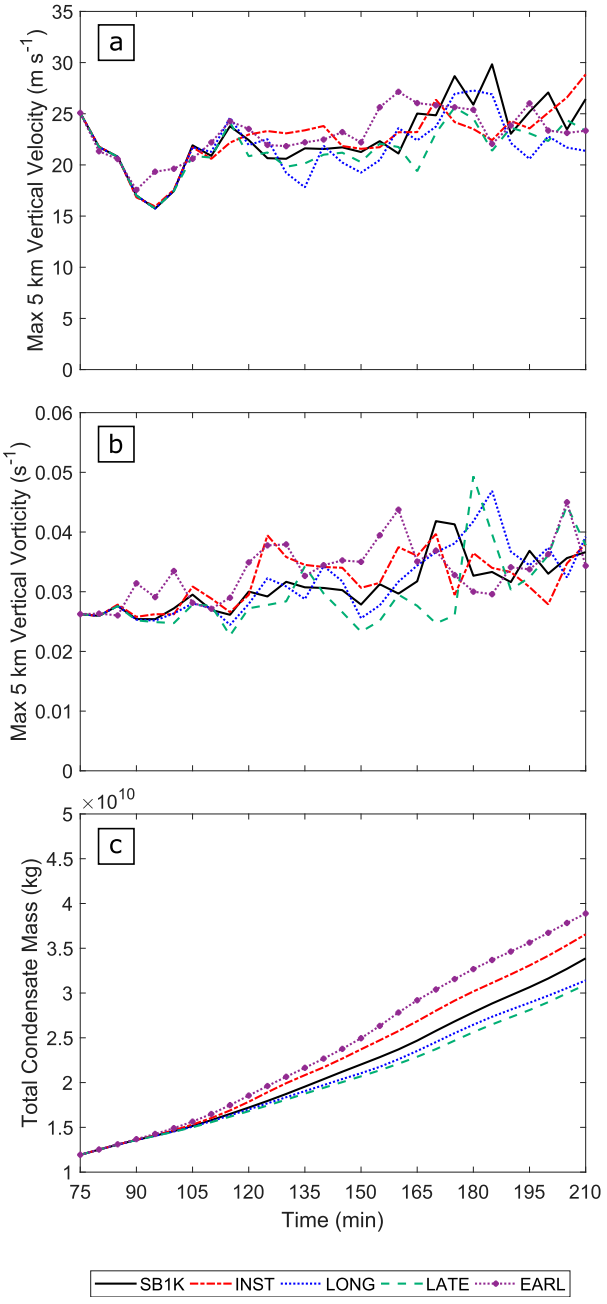

FIG. 13. As in Fig. 6, but for the SB1K (black), INST (red), LONG (blue), LATE (green), and EARL (purple) simulations.

BSS timing or duration is modified, with all simulated storms maintaining a moderate strength updraft for the entire simulation period (Fig. 13a). Both INST and EARL storms are in the full SB air mass earlier than SB1K, so they are subject to the beneficial conditions provided by the opposing low-level winds and increased wind shear for longer, with little effect on longevity relative to SB1K. It may be expected, however, for the LONG or LATE storms to be adversely affected, as the entire SB air mass is influencing their morphology at a later time period, which could be too late in the storm's life cycle for the beneficial lifting to be effective. This is not observed in the present simulations as both storms are still moderately strong multicells when BSS has stopped being applied (not shown). There are small differences in intensity, with both INST and EARL storms more intense than the LONG and LATE storms (Table 5). However, all four storms show an increase in intensity and display characteristics often observed in supercell storms, similar to SB1K (Fig. 13 and Table 5). It would be worthwhile to extend the current results to observe the effect of the SB air mass on storm morphology

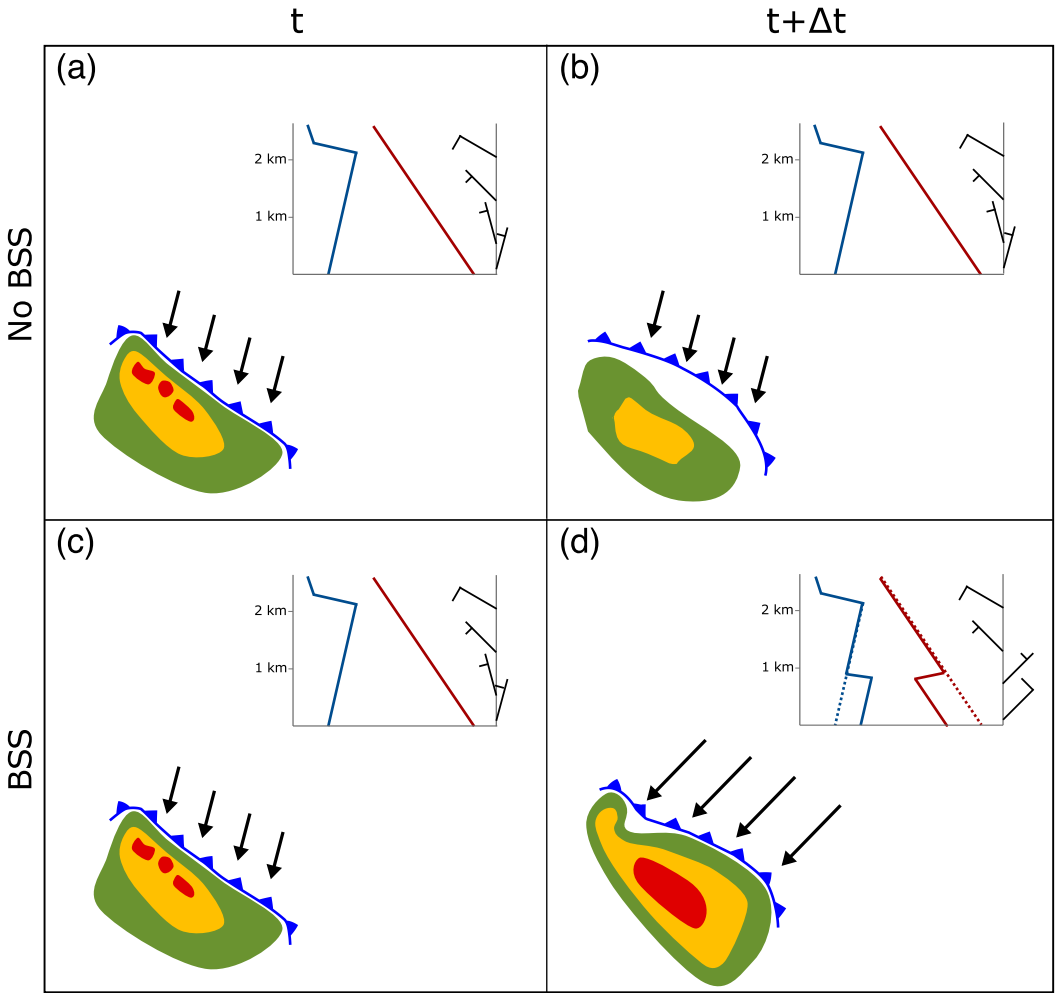

FIG. 14. Summary of the modeling results of the change in storm morphology upon encountering an SB air mass: (a),(c) a mature multicell storm; (b) the multicell storm decaying as it remains in an environment characterized by weak-to-moderate 0–6-km bulk wind difference; and (d) the multicell storm increasing in organization and displaying supercell characteristics after moving into an SB air mass. Storm reflectivity is depicted by the green (weak), yellow (moderate), and red (heavy) filled contours; the storm gust front is depicted by the blue line with triangles; and black arrows depict surface winds ahead of the storm. Idealized boundary layer thermodynamic and wind profiles are provided for the continental air mass in (a)–(c) and the SB air mass in (d). Thick solid lines show the environmental temperature (red) and dewpoint temperature (blue); wind barbs are shown on the right, with short barbs indicating speeds of 5 kt (1 kt $\approx$ 0.51 m s^{-1}) and long barbs indicating speeds of 10 kt. The dotted lines in the SB sounding depict the continental air mass in which the storm originally resided.

for weaker storms, including those that are beginning to dissipate.

4. Summary and future work

During the Australian warm season, preexisting storms moving into an SB air mass sometimes intensify to become particularly severe (e.g., Sills et al. 2004; Richter et al. 2014; Soderholm et al. 2017b). This occasional increase in severity is a concern along the population dense central east coast of Australia, where storms within SB air masses have unexpectedly caused extensive damage. This study explores the impact of the SB air mass on preexisting convective storms forming in an environment characteristic of the central east coast of Australia. Idealized numerical simulations have been performed utilizing the BSS procedure to change the base-state environment to one representative of both a regular SB air mass, and one that has been warmed. In addition, BSS was used to investigate the individual influence of kinematic changes in the SB air mass as opposed to thermodynamic changes.

The results presented in this paper are summarized in Fig. 14. The most important factor behind storm intensification and longevity was found to be the change in the low-level wind field within the air mass. The ambient low-level winds within the SB air mass presented were both stronger and in a direction that is more orthogonal to the storm's gust front when

compared with the continental air mass. This change in low-level shear slowed gust-front propagation, limiting its ability to undercut the updraft and allowing the storm to persist and intensify (Fig. 14d). Further, greater low-level storm-relative inflow supports a continuous connection between the low- and midlevel updraft (Fig. 7) that may assist in overcoming the increased surface-based CIN within the SB air mass. In contrast, if a storm develops in an environment considered marginally supportive of severe convection (Figs. 14a,c) and it does not encounter the SBF and associated air mass, then its gust front will eventually surge ahead of the storm, undercutting the updraft and leading to storm decay (Fig. 14b). A warmed SB air mass was found to produce a more intense storm than an unmodified SB air mass. However, sensitivity tests reveal that the change in wind field within the air mass is required for this increased storm intensity to be realized. These findings contrast with Soderholm et al. (2017b), who hypothesized that boundary layer thermodynamics within the SB air mass are key to storm intensification. However, they are consistent with Lombardo and Colle (2012) and Coffer and Parker (2015), who both demonstrate the importance of low-level shear in sustaining storms that move into a thermodynamically less favorable environment.

Similar to simulations presented by Richardson et al. (2007), storms became increasingly organized when moving into the stronger shear environment represented by the SB air mass. Although specific thresholds for supercell convection were not tested, these storms displayed many characteristics consistent with supercells, including stronger and more persistent updraft rotation, deviant motion to the left of the mean wind vector, a sharp reflectivity gradient along the inflow region of the storm and a v-notch feature. These changes to storm morphology do not appear to be influenced by minor changes in the timing or duration of the BSS procedure, with the only difference being earlier storm intensification and organization when the SB air mass was introduced earlier in the simulation. As an SBF was not simulated in the current study, the results demonstrate that baroclinically generated vorticity along the SBF is not necessary for thunderstorms to transition from multicell to supercell modes, although this process may be important in some cases (e.g., Soderholm et al. 2017b).

The results of this study should not be taken to suggest that every storm moving into an SB air mass such as the one simulated will undergo intensification. Testing the results under different microphysical schemes resulted in the storm decaying before $t = 75$ min, when BSS is applied. After BSS, the storms under different microphysics schemes did not regain strength and continued to decay significantly earlier than the CTRL storm under the Morrison microphysics scheme. This suggests that there would be some sensitivity to cold-pool intensity that was not entirely captured in the experiments presented. BSS only maintains the perturbation fields with respect to the original sounding (Letkewicz et al. 2013). Therefore, cold-pool propagation speeds do not change instantaneously when a cooler background environment is introduced using BSS, as the horizontal density gradient across the gust front is the same. It would be worthwhile conducting further study into the effects of maintaining the full field, rather than the perturbation field.

There are numerous ways in which this work could be built upon. As the simulated storms in this study exhibited updraft rotation, it will be beneficial to assess the relative role of gust-front lifting and dynamical vertical perturbation pressure gradient accelerations in supporting low-level updrafts within the more stable SB air mass, similar to Billings and Parker (2012) and Coffer and Parker (2017). Numerous studies have found at least some updraft parcels continue to be sourced from the boundary layer when it is cooled and stability increases (e.g., Parker 2008; Nowotarski et al. 2011). As such, analysis of updraft parcel paths would provide valuable insights into the relative contribution of parcels sourced from the SB air mass to storm strength. This study did not simulate an SBF; however, future work should focus on the additional influences this might have. Two-dimensional simulations of squall lines by Lombardo and Kading (2018) suggest the inclusion of an SBF may result in further forcing ahead of a preexisting storm that could potentially increase storm severity, especially for those storms in which the gust front begins to surge ahead due to increased outflow. Furthermore, air mass boundaries provide additional horizontal vorticity that can be ingested by a thunderstorm updraft. This study has identified the low-level environmental winds as a primary contributor to storm intensification and longevity. Lericos et al. (2007) found changes to surface roughness affects storm dynamics through changing low-level shear, although this concerned storms moving from the ocean to land, unlike the present study. It is not expected that surface friction would lead to major differences in the results herein; however, inclusion of processes such as friction and surface fluxes in future studies is important to test whether the results hold in more realistic environments. The simulations only tested a small sample of the full parameter space, with the majority of simulations resulting in more intense, long-lived storms after entering the SB air mass, rather than remaining a similar intensity or decaying. This is not always observed, with many real storms decaying after encountering an SB. Further investigation covering a larger portion of the parameter space and incorporating processes such as friction and surface fluxes is required to gain a more complete understanding of the effect of the SBF and its associated air mass on storm morphology and the related hazards for coastal populations.

Acknowledgments. The authors thank Dr. George Bryan for providing and continuing to support CM1 and Dr. Casey Davenport (nèe Letkewicz) for providing the BSS code in CM1. The simulations in this study were performed on the National Computing Infrastructure's Raijin supercomputer. This work was completed as part of the first author's honors degree at the University of Newcastle. We thank Bishnu Lamichhane for acting as local supervisor for the project. Publication support was provided by the Bureau of Meteorology, the School of Earth, Atmosphere and Environment at Monash University, and the School of Mathematical and Physical Sciences at University of Technology Sydney. We thank Matthew Bunkers and two anonymous reviewers for their valuable feedback, which has greatly improved the quality of this paper.

Data availability statement. The CM1 code and input files to run the simulations presented in this paper are available through the Zenodo repository (https://doi.org/10.5281/zenodo.3688837).

REFERENCES

Allen, J., and D. Karoly, 2014: A climatology of Australian severe thunderstorm environments 1979-2011: Inter-annual variability and ENSO influence. *Int. J. Climatol.*, **34**, 81–97, https://doi.org/10.1002/joc.3667.

Atkins, N. T., M. L. Weisman, and L. J. Wicker, 1999: The influence of preexisting boundaries on supercell evolution. *Mon. Wea. Rev.*, **127**, 2910–2927, https://doi.org/10.1175/1520-0493(1999)127<2910:TIOPBO>2.0.CO;2.

Billings, J., and M. Parker, 2012: Evolution and maintenance of the 22–23 June 2003 nocturnal convection during BAMEX. *Wea. Forecasting*, **27**, 279–300, https://doi.org/10.1175/WAF-D-11-00056.1.

Bryan, G. H., 2017: The governing equations for CM1. National Center for Atmospheric Research Tech. Rep., 24 pp., http://www2.mmm.ucar.edu/people/bryan/cm1/cm1.

——, and J. M. Fritsch, 2002: A benchmark simulation for moist nonhydrostatic numerical models. *Mon. Wea. Rev.*, **130**, 2917–2928, https://doi.org/10.1175/1520-0493(2002)130<2917:ABSFMN>2.0.CO;2.

Buckley, B., L. Leslie, and Y. Wang, 2001: The Sydney Hailstorm of April 14, 1999: Synoptic description and numerical simulation. *Meteor. Atmos. Phys.*, **76**, 167–182, https://doi.org/10.1007/s007030170028.

Bunkers, M. J., 2002: Vertical wind shear associated with left-moving supercells. *Wea. Forecasting*, **17**, 845–855, https://doi.org/10.1175/1520-0434(2002)017<0845:VWSAWL>2.0.CO;2.

——, 2010: How midlevel horizontal humidity gradients affect simulated storm morphology. *25th Conf. on Severe Local Storms*, Denver, CO, Amer. Meteor. Soc., P7.1, https://ams.confex.com/ams/25SLS/techprogram/paper_175623.htm.

——, J. S. Johnson, L. J. Czepyha, J. M. Grzywacz, B. A. Klimowski, and M. R. Hjelmfelt, 2006: An observational examination of long-lived supercells. Part II: Environmental conditions and forecasting. *Wea. Forecasting*, **21**, 689–714, https://doi.org/10.1175/WAF952.1.

Coffer, B. E., and M. D. Parker, 2015: Impacts of increasing low-level shear on supercells during the early evening transition. *Mon. Wea. Rev.*, **143**, 1945–1969, https://doi.org/10.1175/MWR-D-14-00328.1.

——, and ——, 2017: Simulated supercells in nontornadic and tornadic VORTEX2 environments. *Mon. Wea. Rev.*, **145**, 149–180, https://doi.org/10.1175/MWR-D-16-0226.1.

Davenport, C. E., and M. D. Parker, 2015: Impact of environmental heterogeneity on the dynamics of a dissipating supercell thunderstorm. *Mon. Wea. Rev.*, **143**, 4244–4277, https://doi.org/10.1175/MWR-D-15-0072.1.

Deardorff, J. W., 1980: Stratocumulus-capped mixed layers derived from a three-dimensional model. *Bound.-Layer Meteor.*, **18**, 495–527, https://doi.org/10.1007/BF00119502.

Doswell, C. I., and E. Rasmussen, 1994: The effect of neglecting the virtual temperature correction on CAPE calculations. *Wea. Forecasting*, **9**, 625–629, https://doi.org/10.1175/1520-0434(1994)009<0625:TEONTV>2.0.CO;2.

Durran, D. R., and J. B. Klemp, 1983: A compressible model for the simulation of moist mountain waves. *Mon. Wea. Rev.*, **111**, 2341–2361, https://doi.org/10.1175/1520-0493(1983)111<2341:ACMFTS>2.0.CO;2.

Houston, A., R. Thompson, and R. Edwards, 2008: The optimal bulk wind differential depth and the utility of the upper-tropospheric storm relative flow for forecasting supercells. *Wea. Forecasting*, **23**, 825–837, https://doi.org/10.1175/2008WAF2007007.1.

Kain, J., and Coauthors, 2008: Some practical considerations regarding horizontal resolution in the first generation of operational convection-allowing NWP. *Wea. Forecasting*, **23**, 931–952, https://doi.org/10.1175/WAF2007106.1.

Klemp, J. B., and R. B. Wilhelmson, 1978: The simulation of three-dimensional convective storm dynamics. *J. Atmos. Sci.*, **35**, 1070–1096, https://doi.org/10.1175/1520-0469(1978)035<1070:TSOTDC>2.0.CO;2.

Lakshmanan, V., B. Herzog, and D. Kingfield, 2015: A method for extracting postevent storm tracks. *J. Appl. Meteor. Climatol.*, **54**, 451–462, https://doi.org/10.1175/JAMC-D-14-0132.1.

Lericos, T., H. Fuelberg, M. Weisman, and A. Watson, 2007: Numerical simulations of the effects of coastlines on the evolution of strong, long-lived squall lines. *Mon. Wea. Rev.*, **135**, 1710–1731, https://doi.org/10.1175/MWR3381.1.

Letkewicz, C. E., A. J. French, and M. D. Parker, 2013: Base-state substitution: An idealized modeling technique for approximating environmental variability. *Mon. Wea. Rev.*, **141**, 3062–3086, https://doi.org/10.1175/MWR-D-12-00200.1.

Lombardo, K., and B. Colle, 2012: Ambient conditions associated with the maintenance and decay of quasi-linear convective systems crossing the northeastern U.S. coast. *Mon. Wea. Rev.*, **140**, 3805–3819, https://doi.org/10.1175/MWR-D-12-00050.1.

——, and T. Kading, 2018: The behavior of squall lines in horizontally heterogeneous coastal environments. *J. Atmos. Sci.*, **75**, 1243–1269, https://doi.org/10.1175/JAS-D-17-0248.1.

Maddox, R., L. Hoxit, and C. Chappell, 1980: A study of tornadic thunderstorm interactions with thermal boundaries. *Mon. Wea. Rev.*, **108**, 322–336, https://doi.org/10.1175/1520-0469(1978)035<1070:TSOTDC>2.0.CO;2.

McAneney, J., D. McAneney, R. Musulin, and G. Walker, 2016: Government-sponsored natural disaster insurance pools: A view from down-under. *Int. J. Disaster Risk Reduct.*, **15**, 1–9, https://doi.org/10.1016/j.ijdrr.2015.11.004.

Miller, S., B. Keim, R. Talbot, and H. Mao, 2003: Sea breeze: Structure, forecasting, and impacts. *Rev. Geophys.*, **41**, 1011, https://doi.org/10.1029/2003RG000124.

Morrison, H., J. A. Curry, and V. I. Khvorostyanov, 2005: A new double-moment microphysics parameterization for application in cloud and climate models. Part I: Description. *J. Atmos. Sci.*, **62**, 1665–1677, https://doi.org/10.1175/JAS3446.1.

Nowotarski, C., P. Markowski, and Y. Richardson, 2011: The characteristics of numerically simulated supercell storms situated over statically stable boundary layers. *Mon. Wea. Rev.*, **139**, 3139–3162, https://doi.org/10.1175/MWR-D-10-05087.1.

Parker, M., 2008: Response of simulated squall lines to low-level cooling. *J. Atmos. Sci.*, **65**, 1323–1341, https://doi.org/10.1175/2007JAS2507.1.

Rasmussen, E., S. Richardson, J. Straka, P. Markowski, and D. Blanchard, 2000: The association of significant tornadoes with a baroclinic boundary on June 2 1995. *Mon. Wea. Rev.*, **128**, 174–191, https://doi.org/10.1175/1520-0493(2000)128<0174:TAOSTW>2.0.CO;2.

Richardson, Y. P., K. K. Droegemeier, and R. P. Davies-Jones, 2007: The influence of horizontal environmental variability on numerically simulated convective storms. Part I: Variations in vertical shear. *Mon. Wea. Rev.*, **135**, 3429–3455, https://doi.org/10.1175/MWR3463.1.

Richter, H., J. Peter, and S. Collis, 2014: Analysis of a destructive wind storm on 16 November 2008 in Brisbane, Australia. *Mon. Wea. Rev.*, **142**, 3038–3060, https://doi.org/10.1175/MWR-D-13-00405.1.

Robinson, F., M. Patterson, and S. Sherwood, 2013: A numerical modeling study of the propagation of idealized sea-breeze density currents. *J. Atmos. Sci.*, **70**, 653–668, https://doi.org/10.1175/JAS-D-12-0113.1.

Sills, D. M. L., J. W. Wilson, P. I. Joes, D. W. Burgess, R. M. Webb, and N. I. Fox, 2004: The 3 November tornadic event during Sydney 2000: Storm evolution and the role of low-level boundaries. *Wea. Forecasting*, **19**, 22–42, https://doi.org/10.1175/1520-0434(2004)019<0022:TNTEDS>2.0.CO;2.

Soderholm, J. S., H. A. McGowan, H. X. Richter, K. Walsh, T. M. Weckwerth, and M. Coleman, 2017a: An 18-year climatology of hailstorm trends and related drivers across southeast Queensland, Australia. *Quart. J. Roy. Meteor. Soc.*, **143**, 1123–1135, https://doi.org/10.1002/qj.2995.

——, ——, ——, ——, T. Wedd, and T. M. Weckwerth, 2017b: Diurnal preconditioning of subtropical coastal convective storm environments. *Mon. Wea. Rev.*, **145**, 3839–3859, https://doi.org/10.1175/MWR-D-16-0330.1.

Trapp, R., G. Marion, and S. Nesbitt, 2017: The regulation of tornado intensity by updraft width. *J. Atmos. Sci.*, **74**, 4199–4211, https://doi.org/10.1175/JAS-D-16-0331.1.

Warren, R. A., H. Richter, H. A. Ramsay, S. T. Siems, and M. J. Manton, 2017: Impact of variations in upper-level shear on simulated supercells. *Mon. Wea. Rev.*, **145**, 2659–2681, https://doi.org/10.1175/MWR-D-16-0412.1.

Weisman, M. L., and J. B. Klemp, 1982: The dependence of numerically simulated convective storms on vertical wind shear and buoyancy. *Mon. Wea. Rev.*, **110**, 504–520, https://doi.org/10.1175/1520-0493(1982)110<0504:TDONSC>2.0.CO;2.

——, and ——, 1984: The structure and classification of numerically simulated convectives storms in directionally varying wind shears. *Mon. Wea. Rev.*, **112**, 2479–2498, https://doi.org/10.1175/1520-0493(1984)112<2479:TSACON>2.0.CO;2.

Wilson, J., and D. Megenhardt, 1997: Thunderstorm initiation, organization, and lifetime associated with Florida boundary layer convergence lines. *Mon. Wea. Rev.*, **125**, 1507–1525, https://doi.org/10.1175/1520-0493(1997)125<1507:TIOALA>2.0.CO;2.

Wissmeier, U., R. Smith, and R. Goler, 2010: The formation of a multicell thunderstorm behind a sea-breeze front. *Quart. J. Roy. Meteor. Soc.*, **136**, 2176–2188, https://doi.org/10.1002/qj.691.

Ziegler, C. L., E. R. Mansell, J. M. Straka, D. R. MacGorman, and D. W. Burgess, 2010: The impact of spatial variations of low-level stability on the life cycle of a simulated supercell storm. *Mon. Wea. Rev.*, **138**, 1738–1766, https://doi.org/10.1175/2009MWR3010.1.